

Multiwavelength observations of KS 1947+300

Wei Liu¹, Pablo Reig^{3,4}, Jingzhi Yan¹, Peng Zhang^{5,6}, Xiukun Li^{1,2}, Bo Gao^{1,2}, Guangcheng Xiao¹, and Qingzhong Liu¹

¹ Key Laboratory of Dark Matter and Space Astronomy, Purple Mountain Observatory, Chinese Academy of Sciences, Nanjing, 210023, P.R. China

² School of Astronomy and Space Science, University of Science and Technology of China, Hefei, 230026, P.R. China

³ Institute of Astrophysics, Foundation for Research and Technology-Hellas, 71110 Heraklion, Greece

⁴ Physics Department, University of Crete, 71003 Heraklion, Greece

⁵ College of Science, China Three Gorges University, Yichang 443002, China

⁶ Center for Astronomy and Space Sciences, China Three Gorges University, Yichang 443002, China

e-mail: a010110288@163.com, jzyan@pmo.ac.cn, zhangpeng@ctgu.edu.cn

Received <date> / Accepted <date>

ABSTRACT

Context. KS 1947+300 is a Be/X-ray binary. Despite its nearly circular orbit, it displays both giant and regular less intense X-ray outbursts. According to the viscous decretion disk model, such low eccentric binaries should not show periodic outbursts.

Aims. We have studied the long-term optical variability of KS 1947+300 and its relationship with X-ray activity. Our objective is to investigate the origin of this variability.

Methods. We have analyzed data covering more than 20 years of observations. In the optical band, we have analyzed spectra and light curves. We measured the strength of the H α and He I 6678 Å lines. In the X-ray band, we studied the long-term light curves provided by several all-sky monitors.

Results. KS 1947+300 exhibits changes in brightness and H α emission on time scales from months to years. The optical and IR variability shows small amplitude changes during the active X-ray state, and a long, smooth decrease during the quiescent state. The fact that the amplitude of variability increased with wavelength suggests that the long-term decrease of the optical emission is due to the weakening of the circumstellar disk. Structural changes in the disk may also be the origin of the periodic signals with periods ~ 200 days detected in the ZTF-*g* and *r* band light curves. We speculate that these changes are related to the mechanism that ejects matter from the photosphere of the Be star into the disk. We have also studied the X-ray variability that manifested as a series of type I outbursts after the two giant outburst in 2000 and 2013 and found that the intensity and peak orbital phase differ from outburst to outburst. The type I outbursts in KS 1947+300 are not strictly periodic. This irregularity could result from precession of the interacting points between the neutron star and the disk, namely the disk apastron and the two nodes of the disk.

Conclusions. The long-term changes in optical continuum and line emission and the X-ray variability patterns are attributed to an evolving and distorted decretion disk.

Key words. stars: emission-line, Be – binaries: close – X-rays: binaries – stars: individual: KS 1947+300 – stars: neutron

1. Introduction

KS 1947+300 was discovered by the *Kvant*/TTM coded-mask X-ray spectrometer on the *Mir* space station on June 8, 1989. At that time, the source reached a peak flux of 70 ± 10 mCrab in the 2–27 keV band; The 1989 giant outburst remained active for 35 days before its X-ray flux dropped below the instrument’s detection limit of 10 mCrab (Borozdin et al. 1990). Studies conducted by Grankin et al. (1991) and Goranskii et al. (1991) revealed that the spectra of the optical counterpart to KS 1947+300 exhibited the H α line in emission, defining KS 1947+300 as a Be/X-ray binary (BeXB). In April 1994, another giant outburst of KS 1947+300 reached a peak flux of 50 mCrab in the 20–75 keV band, lasting for 33 days (Chakrabarty et al. 1995). The system was again bright in X-rays at the end of 2000; In this occasion, the outburst reached a peak flux of 120 mCrab (*RXTE*/*ASM*, 2–10 keV) and lasted for nearly 150 days (Negueruela et al. 2003). The latest giant X-ray outburst occurred in 2013 with a peak flux of 140 mCrab in the 2–20 keV energy band (*MAXI*) and 320 mCrab in the 15–50 keV band (*Swift*-*BAT*), making it one of the

largest giant outburst ever recorded for KS 1947+300. The giant (or type II) X-ray outbursts in December 2000 and October 2013 were followed by a series of normal (type I) outbursts. X-ray pulsations with a pulse period of 18.7579 ± 0.0005 s were detected by Levine & Corbet (2000) and Swank & Morgan (2000) during the normal outbursts in November 2000.

BeXBs are typically divided into persistent and transient sources based on their X-ray long-term variability (Reig 2011). Transient BeXBs display two types of X-ray outbursts: type I (or normal) outbursts and type II (or giant) outbursts. Type I outbursts are regular and (quasi)periodic outbursts, which normally peak at or close to periastron passage of the neutron star, and reach maximum luminosities $L_x \leq 10^{37}$ erg s⁻¹. They tend to cover a relatively small fraction of the orbital period (typically 0.2–0.3 P_{orb}). While, type II outbursts reach luminosities of the order of the Eddington luminosity for a neutron star, $L_x \sim 10^{38}$ erg s⁻¹. Unlike normal outbursts, giant outbursts have no consistently preferred orbital phase and last for a large fraction of an orbital period or even for several orbital periods.

Galloway et al. (2004) obtained an orbital solution for KS 1947+300 with the following orbital parameters: projected semi-major axis $a \times \sin i = 137 \pm 3$ lt-s, orbital period $P_{\text{orb}} = 40.415 \pm 0.010$ d and orbital eccentricity $e = 0.033 \pm 0.013$. Tsygankov & Lutovinov (2005) estimated the magnetic field strength of the neutron star to be 2.5×10^{13} G, based on the correlation of the pulse period derivative and the X-ray luminosity. However, this value of the magnetic field is larger than typical of accreting pulsars ($B \leq 10^{12}$ G) and would imply an unrealistic cyclotron resonant scattering feature at ~ 220 keV. In fact, a cyclotron line at 12.5 keV (i.e. $B \sim 1.1 \times 10^{12}$ G) was reported by Fürst et al. (2014). However, Doroshenko et al. (2020) invoked the low-significance of the residuals and calibration issues to question the reality of that feature. Hence the actual value of the magnetic field remains open.

KS 1947+300 has been observed by many X-ray missions and its X-ray variability has been studied in detail. In contrast, the number of works that study the properties of this system in the optical band reduce to two. Negueruela et al. (2003) presented the first optical spectroscopy and optical and infrared photometry of the counterpart to the transient X-ray source KS 1947+300. They showed it to be a moderately reddened $V = 14.2$ early-type Be star located in an area of low interstellar absorption slightly above the Galactic plane. They derived a spectral type B0Ve and estimated a distance ~ 10 kpc. Kızıloğlu et al. (2007) performed optical photometry of KS 1947+300 with high cadence and found an increase of about 0.1 mag in coincidence with and increase in the X-ray flux from quiescence to 5×10^{36} erg s⁻¹, typical behavior of a type I outburst. Other works that report optical observations of KS 1947+300 in the context of a global study of the optical properties of BeXBs are given in Reig & Fabregat (2015), Reig et al. (2016), and Reig & Fabregat (2022).

In this article, we present the most comprehensive optical analysis of KS 1947+300, including spectroscopic and photometric data from various bands: the infrared bands at 3.4 μm and 4.6 μm , the V -band, the $H\alpha$ line, and the He I $\lambda 6678$ line. Additionally, we provide the X-ray light curve and spin variations of the neutron star for reference. These observations reveal the gradual decrease in the size of the circumstellar disk around the Be star following giant X-ray outbursts. Our main focus is on the changes in the optical band and their connection with the evolution of the circumstellar disk of the Be star.

2. Observations and data analysis

2.1. Optical spectroscopy

Optical spectroscopic observations were obtained from three telescopes at three different observatories: The observations from the Xinglong Station of National Astronomical Observatories in Hebei province (China) were obtained with the spectrometer OptoMechanics Research (OMR) or BAO Faint Object Spectrograph and Camera (BFOSC) on the 2.16 m telescope; while the observations from the Lijiang station of Yunnan Astronomical Observatory in Yunnan province (China) used the spectrometer Yunnan Faint Object Spectrograph and Camera (YFOSC) on the 2.4 m telescope. The OMR is equipped with a 1024×1024 (24 micron) pixels TK1024AB2 CCD. The OMR Grism 4 is 1200 lines mm⁻¹, giving a nominal dispersion of 1.0 \AA pixel⁻¹ and a spectral resolution of 2.7 \AA . The average resolving power is $R \sim 2300$ over the wavelength range of 5500–6900 \AA (Fan et al. 2016). The BFOSC is equipped with a 2048×2048 (15 micron) pixels Loral Lick 3 CCD. The nominal dispersion of

the BFOSC Grism 8 is 1.79 \AA pixel⁻¹, covering the wavelength range of 5800–8280 \AA (Fan et al. 2016). The spectral resolution is about 2.4 \AA ($R \sim 3000$). The YFOSC is equipped with a $2k \times 4k$ (13.5 micron) pixels E2V 42-90 CCD. The nominal dispersion of the YFOSC Grism 8 is 1.47 \AA pixel⁻¹. The spectral resolution is about 10.3 \AA covering the wavelength range of 4970–9830 \AA . The average spectral resolving power is about 700. In addition, we analyzed optical spectroscopic observations obtained from the 1.3 m telescope of the Skinakas observatory (SKO) in Crete (Greece). The 1.3 m telescope was equipped with a 2048×2048 (13.5 micron) pixels ANDOR IKON CCD, a 1302 lines mm⁻¹ grating, and a slit width of 160 μm giving a nominal dispersion of ~ 0.94 \AA pixel⁻¹. The spectral resolving power of the 1.3 m telescope is about 1300, covering the wavelength range of 5400–7300 \AA . Data prior to 2016 were taken from Reig et al. (2016).

We used the Image Reduction and Analysis Facility (IRAF)¹ software package to reduce and analyze all the spectra, including bias-subtracted correction and flat-field correction, and cosmic-ray subtraction. A Helium-Argon calibration lamp was employed to obtain the pixel–wavelength relationship. In order to ensure the consistency of spectral processing, all spectra were normalized to adjacent continua. We measured the equivalent widths of the $H\alpha$ lines (hereafter EW($H\alpha$) for short) for five times, each measurement with a different selection of the continuum. The final EW($H\alpha$) is the average of the five measurements, and the error is the standard deviation. The typical error of EW($H\alpha$) is within 5%. The value of the error is determined by the quality of the continuum. The equivalent widths of the He I $\lambda 6678$ lines (hereafter EW(He I $\lambda 6678$) for short) were obtained following the same method as EW($H\alpha$).

The log of the spectroscopic observations is given in Tables A.1, A.2 & A.3. EW(He I $\lambda 6678$) and EW($H\alpha$) are plotted in the third and sixth panels of Fig. 2, respectively. The evolution of the EW($H\alpha$) is plotted in the third panel of Fig. 1. The evolution of the $H\alpha$ line profiles from 2018 to 2022 is plotted in Fig. 3.

2.2. Optical photometry

Optical photometric observations were obtained from five telescopes at four different observatories: From the Xinglong Station of National Astronomical Observatories, Chinese Academy of Sciences (NAOC), observations were obtained with the Tsinghua-NAOC Telescope (TNT, 80 cm) and the 60 cm telescope; from the Lijiang station of Yunnan Observatories (YNAO), the data came from the 2.4 m telescope; from the Yaoan astronomical observation station of Purple Mountain Observatory (PMO), the data came from the Yaoan High Precision Telescope (YAHPT); from the Skinakas observatory, the data were obtained with the 1.3 m telescope.

The TNT (80 cm) is an equatorial-mounted Cassegrain system with a focal ratio of $f/10$, made by AstroOptik, funded by Tsinghua University in 2004 and jointly operated with NAOC, which is equipped with the PI VersArray 1300B LN 1340×1300 thin, back-illuminated CCD with a 20 μm pixel size (Huang et al. 2012). In this configuration, the plate scale is 0.52" pixel⁻¹ and gives a field of view of 11.5×11.2 arcmin². The 60 cm telescope is an equatorial-mounted system with a focal ratio of $f/4.23$,

¹ IRAF is distributed by NOAO, which is operated by the Association of Universities for Research in Astronomy, Inc., under cooperation with the National Science Foundation.

which is equipped with the Andor DU934P-BEX2-DD 1024 × 1024 CCD and provides a field of view of 18 × 18 arcmin². The 2.4 m telescope is an altazimuth-mounted Cassegrain system with a focal ratio of f/8, which is equipped with the E2V CCD42-90 2k × 2k thin, back-illuminated, deep-depletion CCD with a 13.5 μm pixel size. In this configuration, the plate scale is 0.28" pixel⁻¹ and gives a field of view of 9.6 × 9.6 arcmin². The YAHPT (80 cm') is an altazimuth-mounted, RC optical system with a focal ratio of f/10, made by Astro Systeme Austria, which is equipped with the PIXIS 2048B back-illuminated CCD with a 13.5 μm pixel size. In this configuration, the plate scale is 0.347" pixel⁻¹, providing a field of view of 11.8 × 11.8 arcmin².

Three different CCDs we used during the observations from the Skinkas observatory: Before June 2007, a 1024 × 1024 SITE chip with a 24 μm pixel size (corresponding to 0.5 arcsec on the sky) was used. From July 2007 to October 2017, the telescope was equipped with an ANDOR CCD DZ436. From 2018, an IKON-L 926 was installed. Both have an array of 2048 × 2048 13.5 μm pixel size (corresponding to 0.28 arcsec on sky), hence providing a field of view of 9.5 square arcmin.

In all five telescopes, KS 1947+300 was observed through the standard Johnson-Cousins *B*, *V*, *R*, and *I* filters. The photometric data reduction was performed using standard routines and aperture photometry packages (some from the zphot package) in IRAF, including bias subtraction and flat-field correction. In order to derive the variation in the optical brightness, we selected the reference star C1 (α : 19 49 41.5, δ : +30 13 47, J2000) (according to Reig & Fabregat 2015, the average magnitudes of the reference star are $B = 15.329 \pm 0.006$, $V = 14.504 \pm 0.006$, $R = 14.002 \pm 0.006$, and $I = 13.537 \pm 0.009$) in the field of view of KS 1947+300 to derive its differential magnitudes. In the case of the Skinakas observations, the quoted magnitudes resulted from absolute photometry. Standard stars from the Landolt's list (Landolt 2009) were used for the transformation equations. Observations prior to 2015 were taken from Reig & Fabregat (2015). Observation after that year represent new data. The photometric magnitudes are given in Tables B.1, B.2 & B.3.

The long-term *R*-band light curve is plotted in the second panel of Fig. 1. It covers the period 2000–2023, while the Johnson *V*-band light curve covering the period after the 2013 X-ray outburst is plotted in the fourth panel of Fig. 2. The evolution of the (*B* – *V*) color index is plotted in the fourth panel of Fig. 1 and the seventh panel of Fig. 2.

2.3. ZTF data

The ZTF Observing System is installed on the 48 inch Samuel Oschin Telescope (Schmidt-type) at the Palomar Observatory. It uses 16 e2v 6k x 6k CCD231-C6 CCDs. The 15 microns pixels provide a pixel scale of 1"/pixel and a field of view of 47 square degrees. With this large field of view, ZTF scans the entire Northern sky every two days. ZTF uses three custom made filters, ZTF-g, ZTF-r, and ZTF-i, centered at around 480 nm, 650 nm, and 800 nm, respectively (Bellm et al. 2019).

We downloaded the KS 1947+300 light curves from the Infrared Science Archive (IRSA) ². The data correspond to the ZTF public Data Release (DR) 18 (release on July 07, 2023). The ZTF-*r* and *g* light curves are shown in Figs. 1 and 2.

2.4. NEOWISE data

We made use of the light curves in the W1 (3.4 μm) and W2 (4.6 μm) bands provided by NEOWISE (Mainzer et al. 2011) project through the IRSA viewer³, and plot them in the fifth panel of Fig. 2.

2.5. X-Ray data

The All-Sky Monitor (ASM)^{4,5} on board *RXTE*, BAT ⁶ on board *Swift* (Krimm et al. 2013), *MAXI*⁷, and the Gamma-ray Burst Monitor (GBM)⁸ on board *Fermi* (Meegan et al. 2009) have been monitoring KS 1947+300 in the hard X-ray energy band (2–10 keV with ASM, 15–50 keV with BAT, 2–20 keV with *MAXI*, and 12–50 keV with GBM). Two giant X-ray outbursts and several normal outbursts were detected between 2000 and 2023. The X-ray band light curves from ASM (2–10 keV), BAT (15–50 keV), and *MAXI* (2–20 keV) are plotted in the first panel of Figs. 1 and 2. The spin-frequency history measured by GBM is plotted in the second panel of Fig. 2.

3. Results

The profile changes of emission lines in Be stars, especially of the $H\alpha$ line, can be used to track the dynamic evolution of the Be circumstellar disk (Negueruela et al. 2001). Unfortunately, the spectral resolution of most of our spectra is too low to perform a detailed analysis, but it is still possible to obtain some information from intensity changes in the continuum and line emission.

3.1. Long-term optical variability

The X-ray variability was dominated by two giant (type II) outbursts that took place in 2000 and 2013. They were followed by a series of normal (type I) outbursts, whose peak intensities were roughly modulated by the orbital period. The type I outburst phase was particularly intense from November 2000 to January 2005 and from February 2014 to March 2015. In the optical band, the behavior of the continuum and line emission during the type I active phases in X-rays is similar for the two intervals, although the source was in a fainter state after the 2013 outburst. The optical variability is characterized by a phase of relatively stable emission after the giant outbursts that coincides with the presence of type I outbursts, followed by a decrease in the overall brightness once the X-ray activity ceased (see Fig. 1). This decrease in brightness after the 2013 outburst is more distinctly observed in the *R* and *I* bands than in the *B* and *V* bands: on average the amplitude of variation amounted to 0.15, 0.2, 0.24, and 0.26 mag for the *B*, *V*, *R*, and *I*, respectively. During the same interval, $EW(H\alpha)$ decreased by $\sim 6 \text{ \AA}$.

Figure 2 focuses on the variability after the 2013 major outburst, where we replaced the *R* band with the *V* band, and added the neutron star spin-frequency history and NEOWISE 3.4 μm and 4.6 μm infrared band light curves.

³ <https://irsa.ipac.caltech.edu/irsaviewer>

⁴ ASM consists of three wide-angle shadow cameras equipped with proportional counters with a total collecting area of 90 square cm.

⁵ https://heasarc.gsfc.nasa.gov/FTP/xte/data/archive/ASMProducts/definitive_1dwell/lightcurves/xa_ks1947+300_d1.lc

⁶ <https://swift.gsfc.nasa.gov/results/transients/weak/KS1947p300/>

⁷ http://maxi.riken.jp/star_data/J1949+302/J1949+302.html

⁸ <https://gammarray.nsstc.nasa.gov/gbm/science/pulsars/lightcurves/ks1947.html>

² <https://irsa.ipac.caltech.edu/Missions/ztf.html>

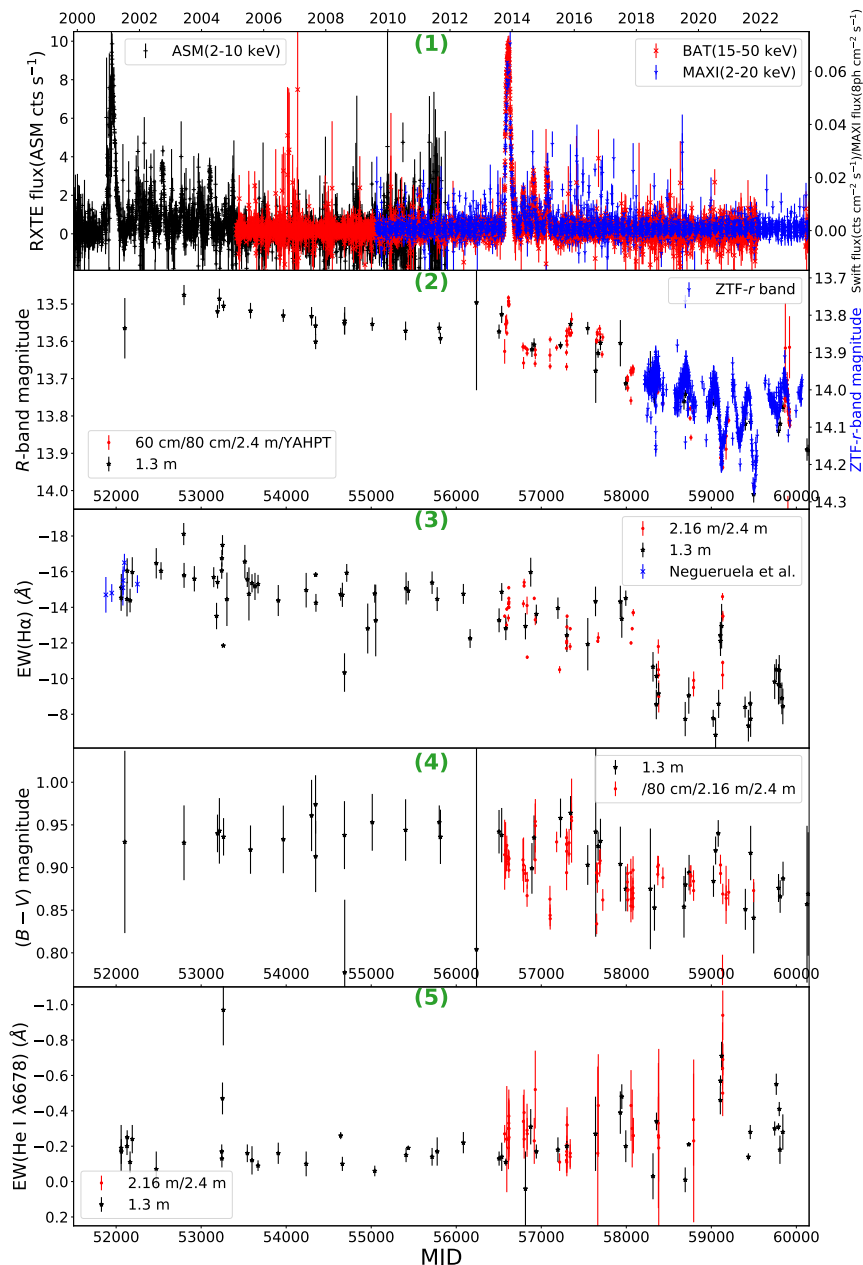


Fig. 1. Panel 1: X-ray light curves. *RXTE*-ASM (2–10 keV), *Swift*-BAT (15–50 keV), and *MAXI* (2–20 keV) are separately labeled with black plus signs, red crosses, and blue downward triangles. The position of the first day of each year is also indicated above panel 1. Panel 2: Long-term light curve of *R*-band. Our data from 60 cm, 80 cm, 2.4 m telescopes, and YAHPT are labeled with red dots. Our data from 1.3 m telescope are labeled with black stars, and the data before 2015 are from Reig & Fabregat (2015). The data from ZTF-*r* band are labeled with blue downward triangles. Panel 3: Long-term variation of $EW(H\alpha)$. Our data from 2.16 m and 2.4 m telescopes are labeled with red dots. Our data from 1.3 m telescope are labeled with black stars, and the data before 2016 are from Reig et al. (2016). And the data from Negueruela et al. (2003) are labeled with blue crosses. Panel 4: Long-term variation of $(B - V)$ color index. Our data from 80 cm and 2.4 m telescopes, and YAHPT are labeled with red dots. Our data from 1.3 m telescope are labeled with black stars, and the data before 2015 are from Reig & Fabregat (2015). Panel 5: Long-term equivalent widths of He I $\lambda 6678$ line. Our data from 2.16 m and 2.4 m telescopes are labeled with red dots. Our data from 1.3 m telescope are labeled with black stars.

In the X-ray band, KS 1947+300 displayed one giant outburst and five normal outbursts from 2013 to 2015, and then it went into a quiescent state. The first, third, and fifth outbursts (number 18, 20, and 22 in Fig. 5) were significantly brighter than the second and fourth ones (number 19 and 21 in Fig. 5). The changes in the neutron star’s spin frequency are very interesting. During the giant outburst, there is a distinct increase in

the spin frequency. The amount of accreted matter transferred enough angular momentum to the neutron star to increase its rotation speed. The spin period decreased from 18.81 s when the outbursts started to 18.78 s at the peak of the outburst. This value appears as some kind of equilibrium period because as soon as the accretion of matter stopped, the spin frequency decreased,

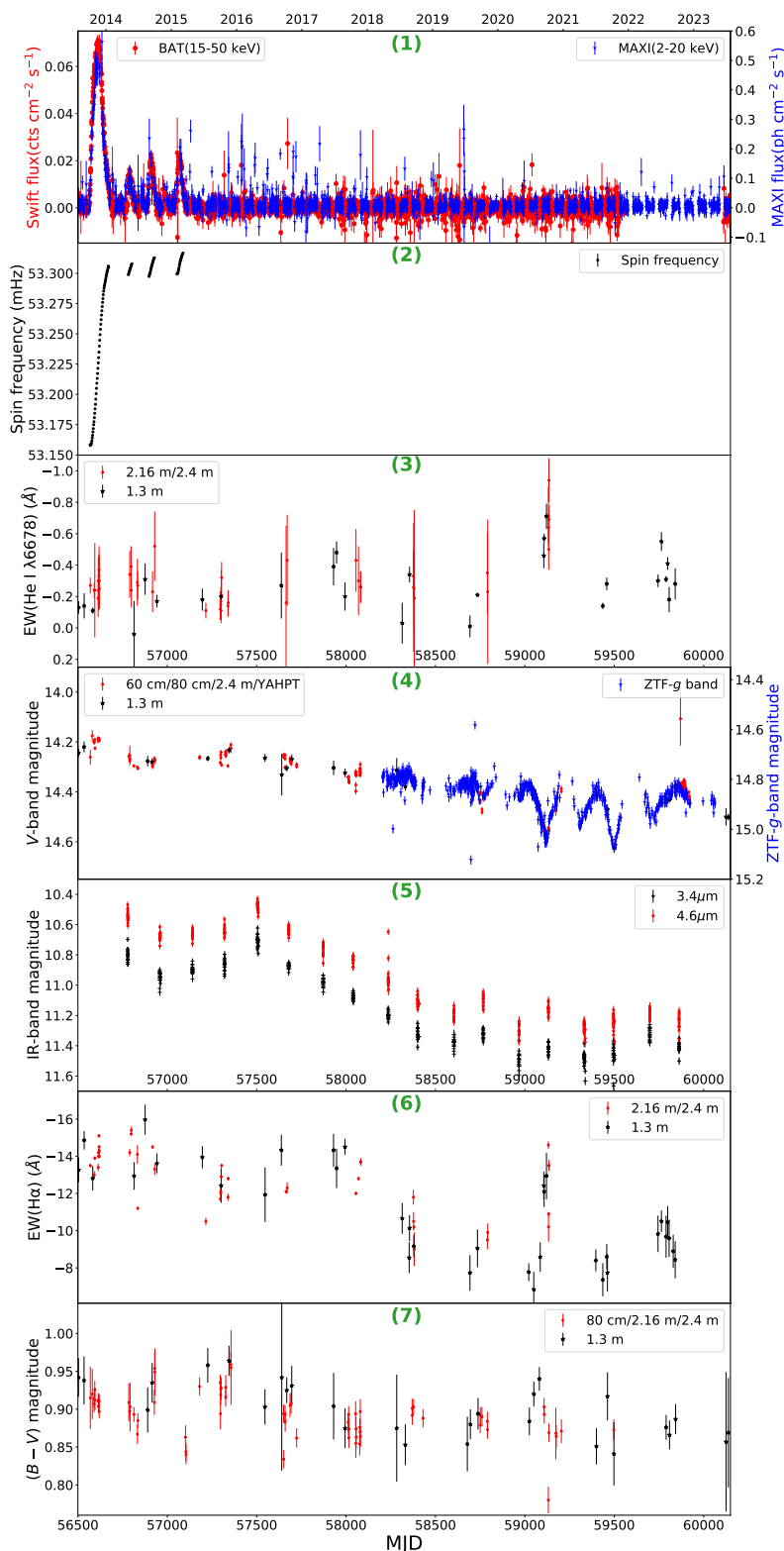
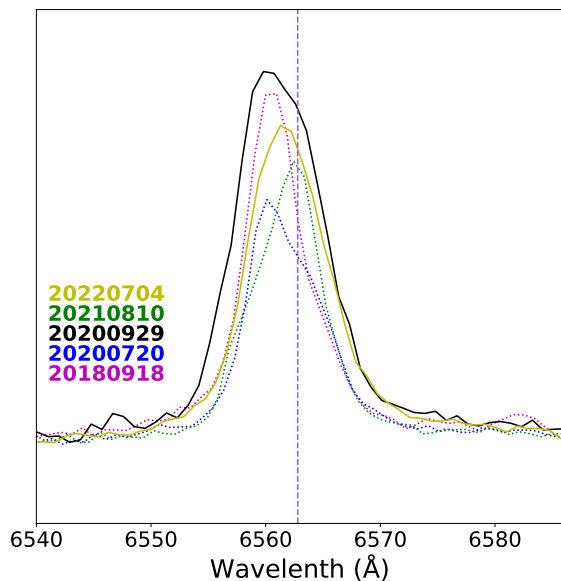


Fig. 2. Panel 1: X-ray light curves. Data from *Swift*-BAT (15–50 keV) and *MAXI* (2–20 keV) are separately labeled with red dots and blue downward triangles. The position of the first day of each year is also indicated above panel 1. Panel 2: Barycentered and orbit-corrected spin-frequency history measured with *Fermi*-GBM. Panel 3: Equivalent widths of He I $\lambda 6678$ line. Our data from 2.16 m and 2.4 m telescopes are labeled with red dots. Our data from 1.3 m telescope are labeled with black stars. Panel 4: Light curves of optical V-band. Our data from 60 cm, 80 cm, 2.4 m telescopes, and YAHPT are labeled with red dots. Our data from 1.3 m telescope are labeled with black stars, and the data before 2015 are from Reig & Fabregat (2015). The data from ZTF-g band are labeled with blue downward triangles. Panel 5: Light curves of infrared 3.4 μm and 4.6 μm bands from *NEOWISE*. They are separately labeled with black plus signs and red dots, respectively. Panel 6: Variation of EW($\text{H}\alpha$). Our data from 2.16 m and 2.4 m telescopes are labeled with red dots. Our data from 1.3 m telescope are labeled with black stars, and the data before 2016 are from Reig et al. (2016). Panel 7: Variation of $(B - V)$ color index. Our data from 80 cm and 2.4 m telescopes, and YAHPT are labeled with red dots. Our data from 1.3 m telescope are labeled with black stars, and the data before 2015 are from Reig & Fabregat (2015).

Table 1. Orbital phases (at the peak) of the series of type I X-ray outbursts after 2000 and after 2013.**Fig. 3.** Evolution of $H\alpha$ line profiles. The vertical lines mark the rest wavelength of the $H\alpha$ line. The dotted line profiles were obtained when the optical brightness was near peak values, while the solid line profiles were obtained when the optical brightness was near valley values.

while it increased again when the accretion rate was large (i.e. during the three brightest type I outbursts).

The IR variability was similar to the optical one, namely small amplitude changes during the active X-ray state, and a long, smooth decrease during the quiescent state.

The He I line at 6678 Å appeared most of the time in emission with its EW(He I λ 6678) stable at -0.3 Å, with small variations. Around October 2020, an abrupt increase was measured in coincidence with a similar increase in EW($H\alpha$).

3.2. Evolution of $H\alpha$ line profiles

The $H\alpha$ line always appears in emission with a broad, sometimes distorted, single peak profile. The low spectral resolution prevents us from a detailed analysis but there is some evidence of V/R variability, which might be the origin of the asymmetry observed in some profiles (i.e. the profile is affected by the precession of a density perturbation in the disk; when it approaches the observer, the intensity increases in the blue part of the profile, while when it moves away from the observer, it affects the red part of the line) (Telting et al. 1994). Figure 3 shows some characteristic profiles of the $H\alpha$ line. These spectra were selected to coincide with the peaks and troughs of the photometric quasiperiodic variability (see Sect. 4.3). However, no significant difference is observed.

4. Discussion

4.1. Changes of circumstellar disk state

Previous works claimed that KS 1947+300 is a Be/X-ray binary whose circumstellar disk's scale is not sensitive to X-ray outbursts. That is to say, the occurrence of X-ray outbursts does not lead to significant changes in the $H\alpha$ line intensity or shape. Negueruela et al. (2003) considered that X-ray outbursts did not

Number	MJD	Phase	Peak Intensity (mCrab)
01	52145	0.96	6.4
02	52190	0.07	6.0
03	52250	0.54	17.6
04	52340	0.78	6.4
05	52410	0.50	10.8
06	52485	0.36	5.6
07	52545	0.86	17.6
08	52645	0.31	8.0
09	52705	0.81	5.6
10	52775	0.53	10.8
11	52860	0.64	5.6
12	52905	0.76	6.8
13	52980	0.60	12.0
14	53105	0.70	16.4
15	53210	0.30	4.8
16	53290	0.28	6.8
17	53370	0.26	12.4
18	56780	0.63	34.6
19	56865	0.74	10.8
20	56915	0.99	49.8
21	56990	0.84	19.5
22	57070	0.82	49.8

have any effect on EW($H\alpha$) because of the low inclination of the system, while Reig et al. (2016) believed that the lack of significant change after the giant X-ray outburst should be attributed to the nearly circular orbit of KS 1947+300. The study presented in this work covers a significant longer time span than previous works and clearly reveal that the state of the circumstellar disk changed in response to the X-ray outbursts, resulting in the fading of the optical and infrared brightness and the decrease of EW($H\alpha$). These changes, however, occur on longer time scales than other well known BeXBs.

The weakening of the line and the fading of the continuum emission started after the 2000 outburst, but accentuated after the 2013 outburst. The decrease in brightness affected more significantly the R and I bands, as well as EW($H\alpha$). This result clearly indicates that the source of the variability is the decretion disk around the Be star. Therefore, we interpret the long-term decrease of the optical emission as a weakening of the disk.

4.2. Study of non-periodic type I X-ray outbursts after 2000 and 2013

After the two giant X-ray outbursts in 1989 and 1994 (Negueruela et al. 2003), KS 1947+300 became active again in late 2000. After the first weak outburst in November 2000 (Levine & Corbet 2000; Swank & Morgan 2000), KS 1947+300 experienced a giant outburst which lasted about 150 days and reached maximum flux around MJD 51953 (February 13, 2001) at more than 120 mCrab (Reig 2008). Subsequently, from the second half of 2001 to the beginning of 2005, the source displayed seventeen normal (type I) outbursts. These outbursts peaked at different intensities and at different time intervals, not exactly coinciding with periastron.

Figures 4 and 5 show the X-ray activity of KS 1947+300 immediately after the giant outbursts in 2000 and 2013, respectively, where the individual outbursts can be discerned. To aid the

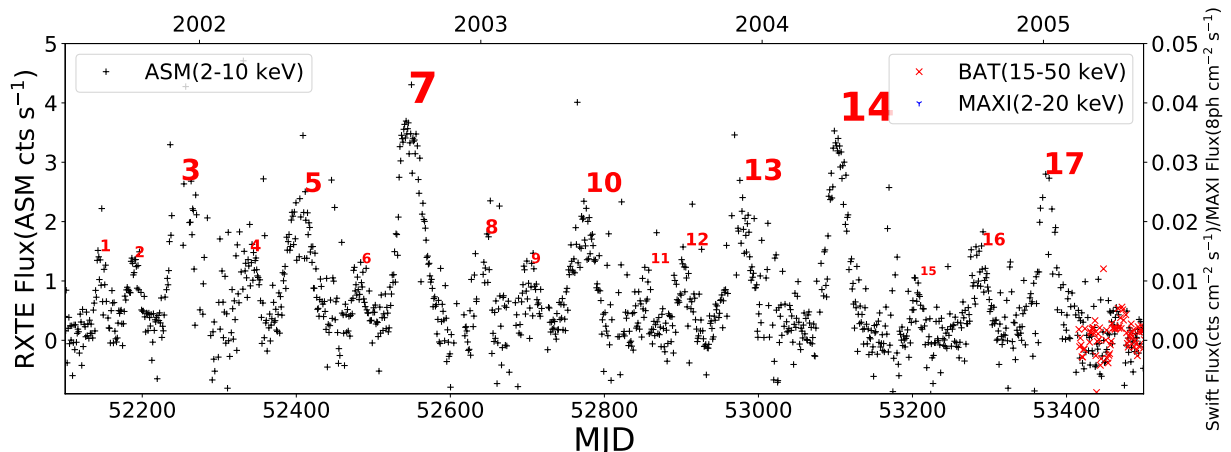


Fig. 4. Schematic diagram of a series of type I X-ray outbursts after 2000. The font size of the type I outburst numbers represents the peak intensity of each outburst.

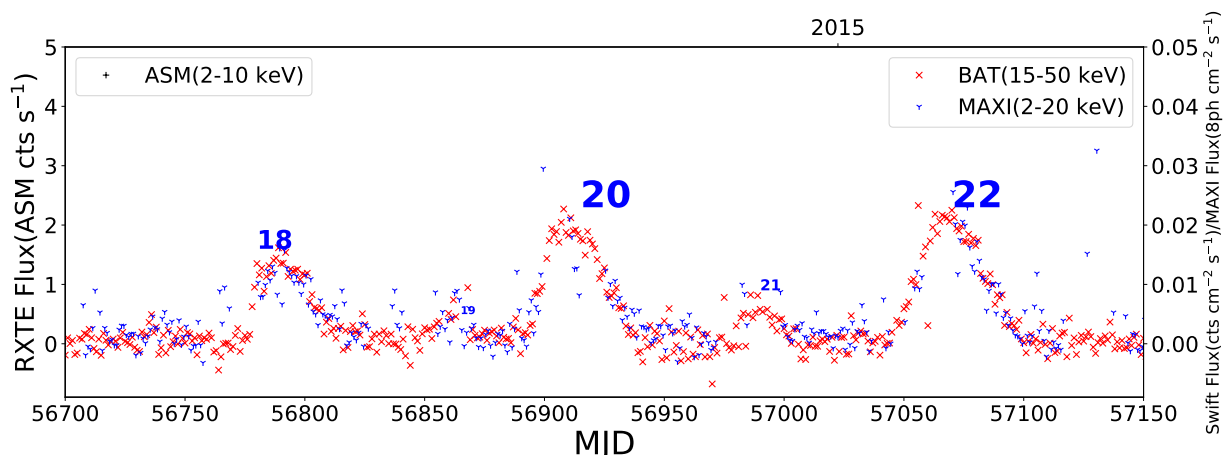


Fig. 5. Schematic diagram of a series of type I X-ray outbursts after 2013. The font size of the type I outburst numbers represents the peak intensity of each outburst.

reader we have marked each outburst with a number in chronological order. These type I outbursts did not occur at a fixed orbital phase, as indicated in Table 1 and Fig. 6. In Fig. 6, the reference point for the orbital phase is taken at $T_{\pi/2}$ (MJD) = 51985.31, with an orbital period of $P_{\text{orb}} = 40.415 \pm 0.010$ d and binary eccentricity 0.033 ± 0.013 (Galloway et al. 2004).

From Fig. 6, it can be observed that although there is no clear preference for orbital phases in these two sets of type I outbursts, nearby outbursts often occurred at similar phases. For example, outbursts number 3 & 5, 6 & 8, 7 & 9, 11 & 13, 12 & 14, 15 & 16 & 17, and 21 & 22 exhibit such behavior.

The main parameters driving the presence of different type of outbursts (type I versus type II) is believed to be the eccentricity of the binary system and viscosity of the disk because these parameters determine the degree of truncation of the disk by the torques exerted by the neutron star. The viscous decretion disk model (Okazaki & Negueruela 2001; Negueruela & Okazaki 2001) predicts that in low eccentric orbits the gap between the disk outer radius and the critical lobe radius of the Be star is so wide that, under normal conditions, the neutron star cannot accrete enough gas at periastron passage to show periodic X-ray outbursts (type I outbursts). In contrast, Be/X-ray binary systems with larger orbital eccentricities are expected to display type I X-ray outbursts more easily because the disk truncation occurs at a much higher resonance radius, which is very close to

or slightly beyond the critical lobe radius at periastron (Okazaki & Negueruela 2001).

However, a number of low eccentric BeXBs have been reported to show type I outbursts (Franchini & Martin 2019, and references therein). The most paradigmatic case is KS 1947+300. Franchini & Martin (2019) found that the extreme mass ratio of the binary leads to the presence of 3:1 Lindblad resonance inside the Be star disk and this drives eccentricity growth. Hence, even in a circular orbit binary, a nearly coplanar disk around the Be star can become eccentric. As a result, the neutron star is able to capture material every time it passes the disk apastron, thus producing type I outbursts.

Another result that challenges the standard view in BeXBs is the fact that type I outbursts in KS 1947+300 are not periodic. Current belief is that type I outbursts are modulated by the orbital period since they normally occur at or near periastron passage. Therefore, the separation between two such outbursts should correspond with the orbital period within some uncertainty. However, we showed (see Fig 6) that KS 1947+300 exhibited type I outbursts at different orbital phases. An explanation for this behavior was provided by Martin & Franchini (2021). They show that nonperiodic type I outbursts may be temporarily driven in a low eccentricity binary with a disk that is inclined sufficiently to be mildly unstable to Kozai–Lidov oscillations, where the inclination and eccentricity of the disk interchange periodically (Mar-

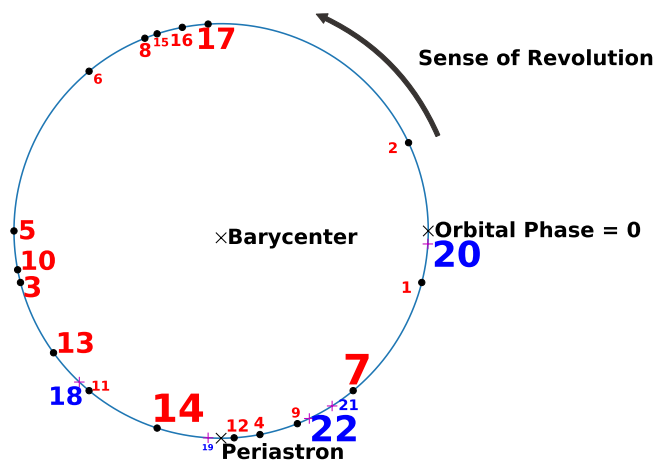


Fig. 6. Orbital phases diagram of a series of type I X-ray outbursts after 2000 and after 2013. The numbers 1–17 represent the type I outbursts after 2000, while the numbers 18–22 represent the type I outbursts after 2013. The font size of the type I outburst numbers represents the peak intensity of each outburst.

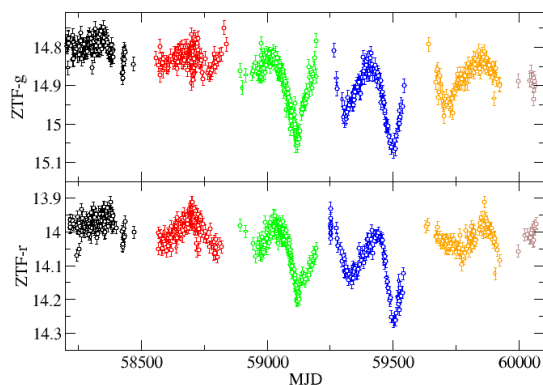


Fig. 7. ZTF-*g* and ZTF-*r* band light curves.

tin et al. 2014; Fu et al. 2015). After several orbital passages of the neutron star, the disk develops an asymmetric structure with one or more spiral arms. Outbursts occur when the neutron star passes close to these spiral arms and pull material from it. The spiral arms may have lower density compared to the circumstellar disk. Therefore, not every accretion event from these arms results in an outburst. According to Martin & Franchini (2021), a misaligned and eccentric disk can have between one and three outbursts per orbit with varying magnitudes depending on the interacting points between the neutron star and the disk. The three different locations would be the disk apastron and the two nodes of the disk (ascending and descending). The irregularity on the outbursts would result from variation of the nodal and apsidal precession.

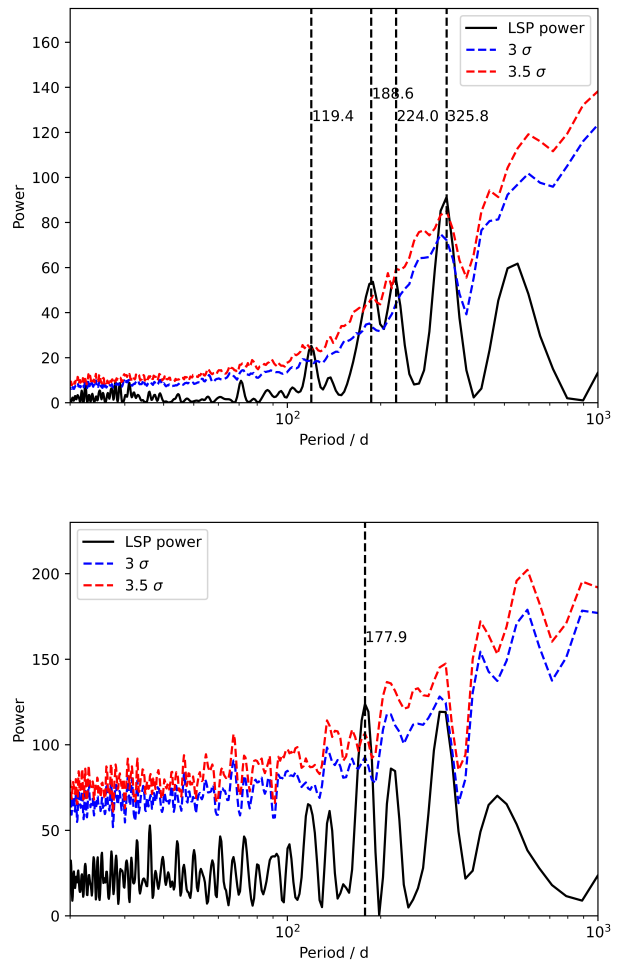


Fig. 8. The LSP results for the ZTF-*g* (upper panel) and ZTF-*r* (lower panel) bands. The black line represents the power values of the LSP. Blue and red dashed lines represent the confidence level curves of 3σ and 3.5σ , respectively. The black dashed line indicates signals that exceed the 3.5σ threshold.

4.3. Periodic signals in ZTF-*g* and *r* band light curves

In Sect. 3, we described the overall long-term variability trends (time scales of years). However, an inspection of Fig. 2 reveals variability in the optical brightness on time scales of months which are particularly apparent when the observation cadence is high (i.e. with the ZTF-*g* and *r* data in the interval 2018–2023). Figure 7 offers a detailed view of these variations.

In order to search for possible periodic signals, we employed the method of Lomb-Scargle periodogram (LSP) (Lomb 1976; Scargle 1982; Zechmeister & Kürster 2009), and estimated the significance of the signals based on their false-alarm probability. We analyzed the data in ZTF-*g* and ZTF-*r* bands and identified several signals with different periods. To estimate the confidence level more robustly, we generate 2×10^4 artificial light curves based on the power spectral density (PSD) and the probability density function of the variation of the ZTF-*g* and ZTF-*r* light curve, respectively (Emmanoulopoulos et al. 2013). The simulated light curves have the full properties of statistics and variability of the ZTF-*g* and ZTF-*r* light curve. By obtaining the LSP periodograms of these simulated light curves, we derive confidence curves at 3σ and 3.5σ levels.

Figure 8 shows the LSP periodograms that resulted from the analysis of the ZTF-*g* band (upper panel) and ZTF-*r* band (lower panel). We have detected four signals that exceed the 3.5σ threshold in the ZTF-*g* light curve. Their corresponding periods are 119.4 ± 5.8 d, 188.6 ± 14.2 d, 224.0 ± 14.2 d and 325.8 ± 23.3 d (the values after the plus/minus sign indicate the full width at half maximum (FWHM) of the peaks), respectively. As for the ZTF-*r* band, we have detected a single signal that exceeded the 3.5σ threshold, with a period value of 177.9 ± 12.1 d. We also detect corresponding periods in ZTF-*r* band similar with that in ZTF-*g* band, but these signals do not exceed the 3.5σ threshold.

The longest period is most likely an artifact of the data, as the spectral window function gives a strong peak at 0.0031 c d^{-1} and can be attributed to the annual restriction in the visibility of the source due to its proximity to the Sun. The shorter period is barely significant and is only detected in the ZTF-*g* band. It could be a subharmonic of the 225 d signal. The other two significant periods correspond to the quasi-sinusoidal variability that is clearly appreciated in Fig. 7. Owing to the irregular sampling of the light curves and the uncertainty involved, these two periodicities probably correspond to the same physical phenomenon.

Periods longer than the orbital period of the binary have been reported for different type of sources, namely ULX pulsars, disk-fed supergiant X-ray binaries (SGXB), and double-periodic variables (Townsend & Charles 2020), BeXBs (Rajoelimanana et al. 2011), wind-fed SGXBs (Corbet & Krimm 2013), and even black-hole binaries (Kotze & Charles 2012). Townsend & Charles (2020) suggested that the most likely cause of the observed linear relationship between the orbital period and super-orbital periods in high-mass X-ray binary systems is the modulation of precessing hotspots or density waves in accretion disk or circumstellar disk by the binary motion. They reported a distinct correlation between orbital and superorbital periods (see Fig. 1 in Townsend & Charles 2020). However, in the case of KS 1947+300, the detected periods do not follow that relationship. For an orbital period of 40 days, a superorbital period of ~ 1000 days should be observed to agree with the correlation between orbital and superorbital periods. Therefore, if the model that attribute the correlation to processes that take place inside the decretion disk is correct, then we conclude that the origin of the periodicities that we detect in the optical light curves of KS 1947+300 must be outside the decretion disk.

An alternative explanation would attribute these periods to some kind of circumbinary motion. Hydrodynamical simulations of the disk evolution in BeXBs showed that most of the material that is lost from the disk is accreted on to the Be star, a small fraction is transferred on to the neutron star and give rise to the X-ray outbursts, and some forms a circumbinary disk around the binary (Franchini & Martin 2019; Martin & Franchini 2021). After several neutron star passages, the decretion disk becomes highly disrupted, with chunks of material more dense than others and/or the formation of a spiral arm. The intensity modulation that we detected could come from the super-orbital motion of a circumbinary material clump or the precession of a spiral arm. A closer look at Fig. 7 reveals that the largest amplitude of variability is caused by a decrease in brightness (rather than by an increase). There is a pedestal level around $g = 14.8$ mag and $r = 13.98$ and drops in brightness of $\sim 0.15 - 0.25$ mag. This behavior points toward the occultation of these structures by the Be star.

A third possibility is that it is the disk itself that evolves. It may evolve in physical size, e.g. it expands and partially dissi-

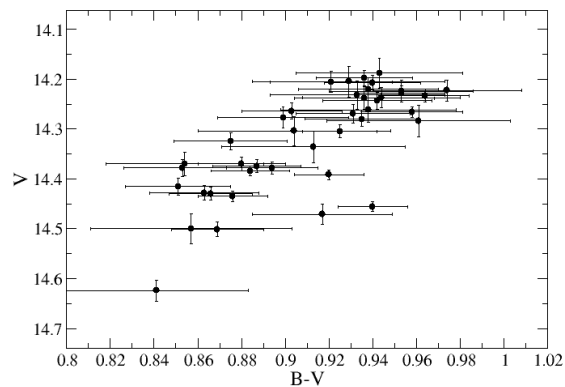


Fig. 9. Relationship between $(B-V)$ color index and V -band magnitude.

pates on time scales of months or in density. In this third scenario we would expect a corresponding increase and decrease in $EW(H\alpha)$. Unfortunately, the spectroscopic observations suffer from numerous gaps. However, Fig. 2 provides a clue that this may indeed be the case. If we compare the evolution of $EW(H\alpha)$ from MJD ~ 59000 with the ZTF light curves, we observe certain correlation with increases in $EW(H\alpha)$ in coincidence with the brightening of the source, e.g. on MJD $\sim 59100-59200$ and MJD $\sim 59700-59800$. This increase in brightness is also seen in the *NEOWISE* near IR data and $EW(\text{He I } \lambda 6678)$. Despite the observational gaps, this quasi-simultaneous changes in the optical and IR continuum and in the line emission of two lines that probe different regions of the decretion disk strongly imply that the origin of the variability is the disk itself.

Our study of KS 1947+300 emphasizes the variable nature of BeXBs in the optical band on all time scales: long (years) as shown in Sect. 3.1, intermediate (weeks to months) as shown in this section, and short (hours to days) as shown by Reig & Fabregat (2022).

4.4. Color-magnitude diagram

Figure 9 illustrates the relationship between the $(B-V)$ color index and the V -band magnitude. This type of plot can be used to constrain the inclination angle of the system (Harmanec 1983). A positive correlation is observed in systems where the optical intensity increases (or equivalently, as $EW(H\alpha)$ increases) and the radiation becomes redder (i.e., $(B-V)$ increases) with the formation of the circumstellar disk. This correlation is believed to be associated with small or moderate inclination angles (Harmanec 1983; Reig & Fabregat 2015).

The high cadence of the ZTF data allows us to investigate the evolution of the source in the color-magnitude diagram (CMD) with more detail and may provide a clue about the relatively large scattering observed in Fig. 9. Figure 10 shows the ZTF-*g* and color-magnitude diagram $(g-r)-r$. The light curve has been divided into six data sets. The gaps are caused by the lack of data due to the proximity of the source to the Sun. The smaller panels in this figure display the location of the source in the CMD for each date set. As in the case of the broad-band Johnson filters, as the source becomes brighter, it also becomes redder. Interestingly, when the source exhibits large amplitude changes in brightness, it performs a complete loop in the CMD, clockwise.

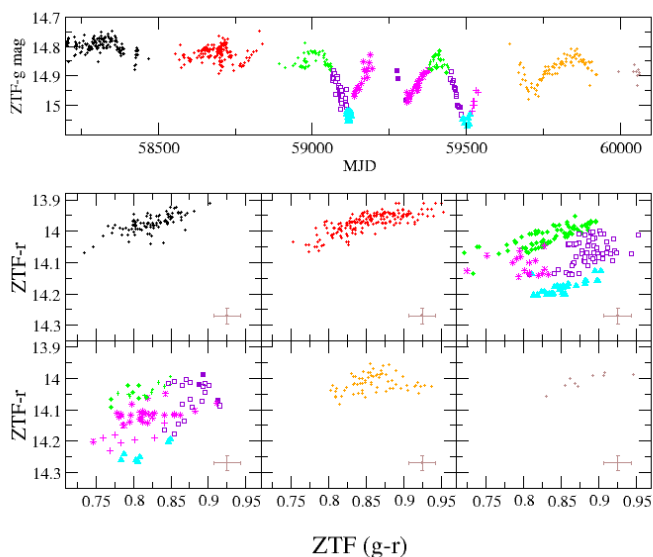


Fig. 10. ZTF light curve and color-magnitude diagram. The top panel shows the light curve of the ZTF-g band. Typical errors are 0.018 mag. The six panels below show the color-magnitude diagram for each individual data set. The color code and symbols in the color-magnitude diagram correspond to those displayed in the light curve.

If we assume that the brightness variability is due to the evolution of the circumstellar disk, as explained in Sect. 4.3, then the declining part would correspond to the dissipation of the disk and the rising part to its growth. The CMD reveals that the emission from the system (star plus disk) is redder during the declining phase (violet square symbols in Fig. 10) and bluer during the rising phase (magenta stars). This result can be understood if the dissipation and subsequent growth starts in the inner parts of the disk.

The disk contribution to the B and V -band emission comes from very close to the star (Haubois et al. 2012). The effective wavelength of the ZTF-g filter is around 4800 Å (i.e. in between Johnson B and V filters), while that of the ZTF-r filter is around 6500 Å (i.e. $\sim R$ band) (Bellm et al. 2019). If the mechanism that ejects matter from the photosphere of the Be star into the disk ceases (dissipation phase), then a hole will be created in the inner parts of the disk and the emission at longer wavelength will dominate. When this mechanism re-starts, the contribution at shorter wavelength will increase (brightening phase).

5. Conclusions

We have studied the evolution of the optical emission of KS 1947+300 since 2000. This long time span allowed us to investigate the X-ray and optical/IR emission in a correlated way. We have shown a long-term fading of the source in the optical/IR band that began after the 2000 X-ray outburst and became more evident after the type II 2013 X-ray outburst. We interpret this decrease of the optical emission as an overall weakening of the decretion disk around the Be star. Surprisingly, in addition to type II X-ray outbursts, KS 1947+300 also displays type I outburst. Because of its nearly circular orbit, KS 1947+300 is not expected to show this kind of periodic outbursts. The fact that we do observe them implies that the disk around the Be star becomes eccentric. As a result, the neutron star is able to capture material when it passes the disk apastron, thus producing type I outbursts. The asymmetric geometric configuration of the disk

may explain the fact that type I outbursts in KS 1947+300 do not show a clear preference for a specific orbital phase (i.e. are not strictly modulated by the orbital period).

We have reported for the first time optical variability on intermediate time scales. KS 1947+300 went through several brightening/fading cycles with characteristic time scales of few months. We studied several scenarios (precession of hot spots or density waves in the decretion disk, circumbinary material clumps), but we concluded that the most likely origin of this variability is changes in the geometrical size of the disk, caused by the temporary halt of the mechanism that ejects material from the photosphere of the Be star into the disk.

Finally, the relationship between the $(B - V)$ color index and the V -band magnitude indicated that the inclination angle of KS 1947+300 is small or moderate.

Acknowledgements. We acknowledge the support of the staff of the Xinglong 2.16m/80cm/60cm telescope. This work was partially supported by the Open Project Program of the Key Laboratory of Optical Astronomy, National Astronomical Observatories, Chinese Academy of Sciences. We acknowledge the support of the staff of the Lijiang 2.4 m telescope. Funding for the telescope has been provided by CAS and the People’s Government of Yunnan Province. Skinakas Observatory is run by the University of Crete and the Foundation for Research and Technology-Hellas. This research has made use of data provided by the Yaoan High Precision Telescope. We acknowledge the Samuel Oschin 48-inch Telescope at the Palomar Observatory as part of the Zwicky Transient Facility project, supported by the National Science Foundation under Grant No. AST-1440341 and a collaboration including Caltech, IPAC, the Weizmann Institute for Science, the Oskar Klein Center at Stockholm University, the University of Maryland, the University of Washington, Deutsches Elektronen-Synchrotron and Humboldt University, Los Alamos National Laboratories, the TANGO Consortium of Taiwan, the University of Wisconsin at Milwaukee, and Lawrence Berkeley National Laboratories. Operations are conducted by COO, IPAC, and UW. This publication makes use of data products from *NEOWISE*, which is a project of the Jet Propulsion Laboratory/California Institute of Technology, funded by the Planetary Science Division of the National Aeronautics and Space Administration. This research has made use of data and results provided by the *ASM/RXTE* teams at MIT and at the *RXTE* SOF and GOF at NASAs GSFC. Data were obtained through the High Energy Astrophysics Science Archive Research Center Online Service, provided by the NASA/Goddard Space Flight Center. This research utilized *MAXI* data provided by RIKEN, JAXA, and the *MAXI* team. *Swift*-BAT transient monitor results provided by the *Swift*-BAT team. *Fermi*-GBM results provided by the Fermi Science Support Center. This work is supported by the National Key R&D Program of China (2021YFA0718500), and the National Natural Science Foundation of China (Grant No U2031205 and 12233002).

References

- Bellm, E. C., Kulkarni, S. R., Graham, M. J., et al. 2019, *PASP*, 131, 018002
- Borozdin, K., Gilfanov, M., Sunyaev, R., et al. 1990, *Soviet Astronomy Letters*, 16, 345
- Chakrabarty, D., Koh, T., Bildsten, L., et al. 1995, *ApJ*, 446, 826
- Corbet, R. H. D. & Krimm, H. A. 2013, *ApJ*, 778, 45
- Doroshenko, R., Piraino, S., Doroshenko, V., & Santangelo, A. 2020, *MNRAS*, 493, 3442
- Emmanoulopoulos, D., McHardy, I. M., & Papadakis, I. E. 2013, *MNRAS*, 433, 907
- Fan, Z., Wang, H., Jiang, X., et al. 2016, *PASP*, 128, 115005
- Franchini, A. & Martin, R. G. 2019, *ApJ*, 881, L32
- Fu, W., Lubow, S. H., & Martin, R. G. 2015, *ApJ*, 807, 75
- Fürst, F., Pottschmidt, K., Wilms, J., et al. 2014, *ApJ*, 784, L40
- Galloway, D. K., Morgan, E. H., & Levine, A. M. 2004, *ApJ*, 613, 1164
- Goranskii, V. P., Esipov, V. F., Lyutyi, V. M., & Shugarov, S. Y. 1991, *Soviet Astronomy Letters*, 17, 399
- Grankin, K. N., Shevchenko, V. S., & Yakubov, S. D. 1991, *Soviet Astronomy Letters*, 17, 415

- Harmanec, P. 1983, *Hvar Observatory Bulletin*, 7, 55
- Haubois, X., Carciofi, A. C., Rivinius, T., Okazaki, A. T., & Bjorkman, J. E. 2012, *ApJ*, 756, 156
- Huang, F., Li, J.-Z., Wang, X.-F., et al. 2012, *Research in Astronomy and Astrophysics*, 12, 1585
- Kızıloğlu, Ü., Baykal, A., & Kızıloğlu, N. 2007, *Astronomische Nachrichten*, 328, 142
- Kotze, M. M. & Charles, P. A. 2012, *MNRAS*, 420, 1575
- Krimm, H. A., Holland, S. T., Corbet, R. H. D., et al. 2013, *ApJS*, 209, 14
- Landolt, A. U. 2009, *AJ*, 137, 4186
- Levine, A. & Corbet, R. 2000, *IAU Circ.*, 7523, 2
- Lomb, N. R. 1976, *Ap&SS*, 39, 447
- Mainzer, A., Bauer, J., Grav, T., et al. 2011, *ApJ*, 731, 53
- Martin, R. G. & Franchini, A. 2021, *ApJ*, 922, L37
- Martin, R. G., Nixon, C., Lubow, S. H., et al. 2014, *ApJ*, 792, L33
- Meegan, C., Lichti, G., Bhat, P. N., et al. 2009, *ApJ*, 702, 791
- Negueruela, I., Israel, G. L., Marco, A., Norton, A. J., & Speziali, R. 2003, *A&A*, 397, 739
- Negueruela, I. & Okazaki, A. T. 2001, *A&A*, 369, 108
- Negueruela, I., Okazaki, A. T., Fabregat, J., et al. 2001, *A&A*, 369, 117
- Okazaki, A. T. & Negueruela, I. 2001, *A&A*, 377, 161
- Rajoelimanana, A. F., Charles, P. A., & Udalski, A. 2011, *MNRAS*, 413, 1600
- Reig, P. 2008, *A&A*, 489, 725
- Reig, P. 2011, *Ap&SS*, 332, 1
- Reig, P. & Fabregat, J. 2015, *A&A*, 574, A33
- Reig, P. & Fabregat, J. 2022, *A&A*, 667, A18
- Reig, P., Nersesian, A., Zezas, A., Gkouvelis, L., & Coe, M. J. 2016, *A&A*, 590, A122
- Scargle, J. D. 1982, *ApJ*, 263, 835
- Swank, J. & Morgan, E. 2000, *IAU Circ.*, 7531, 4
- Telting, J. H., Heemskerk, M. H. M., Henrichs, H. F., & Savonije, G. J. 1994, *A&A*, 288, 558
- Townsend, L. J. & Charles, P. A. 2020, *MNRAS*, 495, 139
- Tsygankov, S. S. & Lutovinov, A. A. 2005, *Astronomy Letters*, 31, 88
- Zechmeister, M. & Kürster, M. 2009, *A&A*, 496, 577

Appendix A: Tables of spectroscopic observations

Appendix B: Tables of photometric observations

Table A.1. Spectroscopic observations of KS 1947+300 from 2.16 m and 2.4 m telescopes.

Date (DD-MM-YYYY)	MJD	Telescope/ Instrument	Wavelength Range (Å)	EW(H α) (Å)	EW(He I λ 6678) (Å)
04-10-2013	56569.5298	2.16 m/BFOSC	3000–8600	-13.5 \pm 0.1	-0.27 \pm 0.05
26-10-2013	56591.4709	2.16 m/OMR	5500–6900	-13.0 \pm 0.2	-0.24 \pm 0.05
29-10-2013	56594.4809	2.16 m/OMR	5500–6900	-13.9 \pm 0.1	-0.24 \pm 0.30
17-11-2013	56613.4826	2.4 m/YFOSC	4970–9830	-13.4 \pm 0.2	-0.19 \pm 0.12
18-11-2013	56614.5221	2.4 m/YFOSC	4970–9830	-14.0 \pm 0.1	-0.30 \pm 0.15
19-11-2013	56615.5067	2.4 m/YFOSC	4970–9830	-14.2 \pm 0.2	-0.24 \pm 0.13
20-11-2013	56616.5489	2.4 m/YFOSC	4970–9830	-14.2 \pm 0.1	-0.30 \pm 0.14
21-11-2013	56617.5169	2.4 m/YFOSC	4970–9830	-15.1 \pm 0.1	-0.33 \pm 0.14
22-11-2013	56618.5163	2.4 m/YFOSC	4970–9830	-14.5 \pm 0.1	-0.37 \pm 0.15
23-11-2013	56619.5049	2.4 m/YFOSC	4970–9830	-14.3 \pm 0.1	-0.30 \pm 0.16
24-11-2013	56620.5087	2.4 m/YFOSC	4970–9830	-14.0 \pm 0.1	-0.25 \pm 0.13
12-05-2014	56789.8602	2.4 m/YFOSC	4970–9830	-14.2 \pm 0.2	-0.34 \pm 0.15
20-05-2014	56797.7249	2.16 m/BFOSC	5800–8280	-15.2 \pm 0.1	-0.39 \pm 0.13
21-05-2014	56798.7677	2.16 m/BFOSC	5800–8280	-15.4 \pm 0.2	-0.24 \pm 0.11
24-06-2014	56832.6864	2.4 m/YFOSC	4970–9830	-14.1 \pm 0.5	-0.29 \pm 0.15
26-06-2014	56834.6520	2.4 m/YFOSC	4970–9830	-11.2 \pm 0.1	-0.27 \pm 0.09
17-09-2014	56917.5525	2.16 m/OMR	5500–6900	-14.5 \pm 0.1	-0.23 \pm 0.13
29-09-2014	56929.5746	2.16 m/OMR	5500–6900	-13.3 \pm 0.3	-0.52 \pm 0.22
12-07-2015	57215.5852	2.16 m/BFOSC	5800–8280	-10.5 \pm 0.2	-0.11 \pm 0.05
01-10-2015	57296.5719	2.16 m/BFOSC	5800–8280	-11.7 \pm 0.1	-0.12 \pm 0.07
03-10-2015	57298.5649	2.16 m/BFOSC	4000–6670	-12.0 \pm 0.4	-0.15 \pm 0.08
04-10-2015	57299.5482	2.16 m/BFOSC	5800–8280	-12.1 \pm 0.1	-0.17 \pm 0.09
05-10-2015	57300.5707	2.16 m/BFOSC	5800–8280	-12.4 \pm 0.1	-0.11 \pm 0.08
06-10-2015	57301.5581	2.16 m/BFOSC	5800–8280	-12.9 \pm 0.1	-0.21 \pm 0.16
08-10-2015	57303.5513	2.16 m/BFOSC	5800–8280	-13.5 \pm 0.1	-0.32 \pm 0.10
13-11-2015	57339.5946	2.4 m/YFOSC	4970–9830	-11.8 \pm 0.2	-0.14 \pm 0.07
14-11-2015	57340.5625	2.4 m/YFOSC	4970–9830	-12.8 \pm 0.1	-0.16 \pm 0.08
03-10-2016	57664.5125	2.16 m/OMR	5500–6900	-12.1 \pm 0.1	-0.16 \pm 0.49
09-10-2016	57670.5324	2.16 m/OMR	5500–6900	-12.3 \pm 0.3	-0.43 \pm 0.29
29-10-2017	58055.4855	2.16 m/OMR	5500–6900	-12.0 \pm 0.1	-0.43 \pm 0.20
12-11-2017	58069.4499	2.16 m/OMR	5500–6900	-12.8 \pm 0.1	-0.30 \pm 0.22
23-11-2017	58080.5023	2.4 m/YFOSC	4970–9830	-13.7 \pm 0.1	-0.26 \pm 0.10
25-11-2017	58082.4982	2.4 m/YFOSC	4970–9830	-13.7 \pm 0.2	-0.26 \pm 0.10
15-09-2018	58376.5708	2.16 m/OMR	5500–6900	-11.8 \pm 0.4	-0.33 \pm 0.15
16-09-2018	58377.5410	2.16 m/OMR	5500–6900	-10.5 \pm 0.5	-0.26 \pm 0.41
18-09-2018	58379.5969	2.16 m/OMR	5500–6900	-10.2 \pm 0.1	-0.25 \pm 0.25
20-09-2018	58381.5586	2.16 m/OMR	5500–6900	-9.0 \pm 0.9	-0.19 \pm 0.56
03-11-2019	58790.5159	2.16 m/OMR	5500–6900	-9.5 \pm 0.5	-0.35 \pm 0.26
05-11-2019	58792.5174	2.16 m/OMR	5500–6900	-9.9 \pm 0.5	-0.23 \pm 0.46
09-10-2020	59131.5513	2.16 m/BFOSC	5800–8280	-14.6 \pm 0.2	-0.71 \pm 0.19
10-10-2020	59132.6247	2.16 m/BFOSC	5800–8280	-10.2 \pm 0.8	-0.64 \pm 0.09
11-10-2020	59133.5878	2.16 m/BFOSC	5800–8280	-10.9 \pm 0.1	-0.50 \pm 0.13
12-10-2020	59134.5923	2.16 m/BFOSC	5800–8280	-13.5 \pm 0.3	-0.94 \pm 0.14
13-10-2020	59135.4988	2.16 m/BFOSC	5800–8280	-13.5 \pm 0.2	-0.69 \pm 0.09

Table A.2. Spectroscopic observations of KS 1947+300 from the 1.3 m telescope (Skinakas observatory).

Date (DD-MM-YYYY)	MJD	Telescope	Wavelength Range (Å)	EW(H α) (Å)	EW(He I λ 6678) (Å)
30-05-2001	52059	1.3 m	5400–7300	-14.53 \pm 0.73	-0.19 \pm 0.13
01-06-2001	52061	1.3 m	5400–7300	-15.10 \pm 0.77	-0.17 \pm 0.07
07-08-2001	52128	1.3 m	5400–7300	-14.46 \pm 0.97	-0.20 \pm 0.05
09-08-2001	52130	1.3 m	5400–7300	-16.05 \pm 0.70	-0.25 \pm 0.04
12-09-2001	52164	1.3 m	5400–7300	-14.38 \pm 0.66	-0.11 \pm 0.06
08-10-2001	52190	1.3 m	5400–7300	-15.97 \pm 0.84	-0.24 \pm 0.08
17-07-2002	52472	1.3 m	5400–7300	-16.47 \pm 0.85	-0.07 \pm 0.10
11-09-2002	52528	1.3 m	5400–7300	-16.04 \pm 0.49	...
05-06-2003	52795	1.3 m	5400–7300	-18.11 \pm 0.62	...
09-06-2003	52799	1.3 m	5400–7300	-15.79 \pm 0.70	...
08-10-2003	52920	1.3 m	5400–7300	-15.60 \pm 0.71	...
23-05-2004	53148	1.3 m	5400–7300	-15.69 \pm 0.56	...
25-06-2004	53181	1.3 m	5400–7300	-13.51 \pm 0.74	...
07-07-2004	53193	1.3 m	5400–7300	-15.41 \pm 0.36	...
25-08-2004	53242	1.3 m	5400–7300	-16.06 \pm 0.46	-0.17 \pm 0.04
27-08-2004	53244	1.3 m	5400–7300	-16.75 \pm 0.47	-0.13 \pm 0.05
03-09-2004	53251	1.3 m	5400–7300	-17.49 \pm 0.56	-0.47 \pm 0.09
13-09-2004	53261	1.3 m	5400–7300	-11.85 \pm 0.05	-0.97 \pm 0.20
25-10-2004	53303	1.3 m	5400–7300	-14.45 \pm 1.50	...
24-05-2005	53514	1.3 m	5400–7300	-16.56 \pm 0.94	...
22-06-2005	53543	1.3 m	5400–7300	-15.56 \pm 0.42	-0.16 \pm 0.05
11-07-2005	53562	1.3 m	5400–7300	-14.75 \pm 1.49	...
16-08-2005	53598	1.3 m	5400–7300	-15.35 \pm 0.51	-0.12 \pm 0.08
20-09-2005	53633	1.3 m	5400–7300	-15.17 \pm 0.76	...
26-10-2005	53669	1.3 m	5400–7300	-15.30 \pm 0.52	-0.09 \pm 0.03
21-06-2006	53907	1.3 m	5400–7300	-14.38 \pm 0.87	-0.16 \pm 0.06
15-05-2007	54235	1.3 m	5400–7300	-14.96 \pm 0.97	-0.10 \pm 0.07
04-09-2007	54347	1.3 m	5400–7300	-15.83 \pm 0.13	...
07-09-2007	54350	1.3 m	5400–7300	-14.25 \pm 0.50	...
24-06-2008	54641	1.3 m	5400–7300	-14.73 \pm 0.36	-0.26 \pm 0.02
14-07-2008	54661	1.3 m	5400–7300	-14.70 \pm 0.68	-0.10 \pm 0.04
08-08-2008	54686	1.3 m	5400–7300	-10.34 \pm 1.08	...
03-09-2008	54712	1.3 m	5400–7300	-15.93 \pm 0.50	...
08-05-2009	54959	1.3 m	5400–7300	-12.81 \pm 1.40	...
30-07-2009	55042	1.3 m	5400–7300	-14.77 \pm 0.51	-0.06 \pm 0.03
10-08-2009	55053	1.3 m	5400–7300	-13.26 \pm 2.01	...
02-08-2010	55410	1.3 m	5400–7300	-15.06 \pm 0.90	-0.15 \pm 0.04
28-08-2010	55436	1.3 m	5400–7300	-14.93 \pm 0.55	-0.19 \pm 0.01
04-06-2011	55716	1.3 m	5400–7300	-15.38 \pm 0.63	-0.14 \pm 0.05
03-08-2011	55776	1.3 m	5400–7300	-14.46 \pm 0.67	-0.17 \pm 0.08
06-06-2012	56084	1.3 m	5400–7300	-14.75 \pm 0.56	-0.22 \pm 0.06
24-08-2012	56163	1.3 m	5400–7300	-12.25 \pm 0.53	...
31-07-2013	56504	1.3 m	5400–7300	-13.27 \pm 0.67	-0.13 \pm 0.04
31-08-2013	56535	1.3 m	5400–7300	-14.86 \pm 0.50	-0.14 \pm 0.08
18-10-2013	56583	1.3 m	5400–7300	-12.82 \pm 0.66	-0.11 \pm 0.02
06-06-2014	56814	1.3 m	5400–7300	-12.94 \pm 0.74	0.04 \pm 0.21
07-08-2014	56876	1.3 m	5400–7300	-15.97 \pm 0.81	-0.31 \pm 0.10
12-10-2014	56942	1.3 m	5400–7300	-13.62 \pm 0.53	-0.17 \pm 0.04
23-06-2015	57196	1.3 m	5400–7300	-13.95 \pm 0.60	-0.18 \pm 0.07
06-10-2015	57301	1.3 m	5400–7300	-12.43 \pm 0.94	-0.20 \pm 0.03
08-06-2016	57547	1.3 m	5400–7300	-11.93 \pm 1.47	...
07-09-2016	57638	1.3 m	5400–7300	-14.33 \pm 0.83	-0.27 \pm 0.21
26-06-2017	57930	1.3 m	5400–7300	-14.32 \pm 0.89	-0.39 \pm 0.12
13-07-2017	57947	1.3 m	5400–7300	-13.35 \pm 1.06	-0.48 \pm 0.07
29-08-2017	57994	1.3 m	5400–7300	-14.51 \pm 0.43	-0.20 \pm 0.09
15-07-2018	58314	1.3 m	5400–7300	-10.66 \pm 0.83	-0.03 \pm 0.13
23-08-2018	58353	1.3 m	5400–7300	-8.55 \pm 0.83	...
25-08-2018	58355	1.3 m	5400–7300	-10.14 \pm 0.70	-0.34 \pm 0.05

Table A.3. Spectroscopic observations of KS 1947+300 from the 1.3 m telescope (Skinakas observatory)–continued.

Date (DD-MM-YYYY)	MJD	Telescope	Wavelength Range (Å)	EW(H α) (Å)	EW(He I λ 6678) (Å)
18-09-2018	58379	1.3 m	5400–7300	-9.16 \pm 0.60	...
29-07-2019	58693	1.3 m	5400–7300	-7.73 \pm 0.96	-0.01 \pm 0.07
09-09-2019	58735	1.3 m	5400–7300	-9.05 \pm 1.02	-0.21 \pm 0.01
22-06-2020	59022	1.3 m	5400–7300	-7.77 \pm 0.48	-2.03 \pm 0.02
20-07-2020	59050	1.3 m	5400–7300	-6.84 \pm 0.95	...
25-08-2020	59086	1.3 m	5400–7300	-8.58 \pm 0.79	...
14-09-2020	59106	1.3 m	5400–7300	-12.42 \pm 0.76	-0.46 \pm 0.08
16-09-2020	59108	1.3 m	5400–7300	-12.11 \pm 0.84	-0.57 \pm 0.03
29-09-2020	59121	1.3 m	5400–7300	-12.94 \pm 1.25	-0.71 \pm 0.08
02-07-2021	59397	1.3 m	5400–7300	-8.40 \pm 0.59	...
10-08-2021	59436	1.3 m	5400–7300	-7.36 \pm 0.89	-0.14 \pm 0.02
01-09-2021	59458	1.3 m	5400–7300	-8.60 \pm 0.68	-0.28 \pm 0.04
05-09-2021	59462	1.3 m	5400–7300	-7.74 \pm 1.01	...
15-06-2022	59745	1.3 m	5400–7300	-9.83 \pm 0.98	-0.30 \pm 0.04
04-07-2022	59764	1.3 m	5400–7300	-10.51 \pm 0.58	-0.55 \pm 0.06
30-07-2022	59790	1.3 m	5400–7300	-9.68 \pm 1.13	-0.31 \pm 0.02
08-08-2022	59799	1.3 m	5400–7300	-10.47 \pm 0.85	-0.41 \pm 0.04
16-08-2022	59807	1.3 m	5400–7300	-9.59 \pm 1.00	-0.18 \pm 0.08
08-09-2022	59830	1.3 m	5400–7300	-8.89 \pm 0.89	...
19-09-2022	59841	1.3 m	5400–7300	-8.44 \pm 1.00	-0.28 \pm 0.10

Table B.1. Photometric observations of KS 1947+300 from the 1.3 m telescope (Skinakas observatory).

Date (DD-MM-YYYY)	MJD	Telescope	<i>B</i> (mag)	<i>V</i> (mag)	<i>R</i> (mag)	<i>I</i> (mag)
11-07-2001	52102.323	1.3 m	15.175 ± 0.073	14.245 ± 0.078	13.565 ± 0.081	12.925 ± 0.077
07-06-2003	52798.393	1.3 m	15.134 ± 0.031	14.205 ± 0.031	13.476 ± 0.027	...
05-07-2004	53192.303	1.3 m	15.147 ± 0.017	14.207 ± 0.014	13.520 ± 0.017	12.857 ± 0.022
27-07-2004	53214.473	1.3 m	15.131 ± 0.024	14.188 ± 0.030	13.486 ± 0.027	12.808 ± 0.041
14-09-2004	53263.322	1.3 m	15.134 ± 0.015	14.198 ± 0.016	13.505 ± 0.014	12.812 ± 0.026
28-07-2005	53580.455	1.3 m	15.127 ± 0.019	14.206 ± 0.021	13.518 ± 0.021	...
18-08-2006	53966.400	1.3 m	15.165 ± 0.027	14.232 ± 0.029	13.531 ± 0.017	...
16-07-2007	54298.392	1.3 m	15.245 ± 0.028	14.284 ± 0.031	13.533 ± 0.025	12.924 ± 0.029
01-09-2007	54345.481	1.3 m	15.197 ± 0.027	14.223 ± 0.021	13.558 ± 0.025	12.877 ± 0.041
02-09-2007	54346.331	1.3 m	15.249 ± 0.028	14.336 ± 0.031	13.601 ± 0.020	12.902 ± 0.021
06-08-2008	54685.528	1.3 m	15.200 ± 0.031	14.262 ± 0.025	13.552 ± 0.029	12.870 ± 0.032
09-08-2008	54688.302	1.3 m	15.091 ± 0.054	14.314 ± 0.066	13.545 ± 0.037	12.862 ± 0.039
29-06-2009	55012.405	1.3 m	15.177 ± 0.025	14.224 ± 0.022	13.554 ± 0.018	12.866 ± 0.018
26-07-2010	55404.362	1.3 m	15.181 ± 0.030	14.237 ± 0.020	13.572 ± 0.025	12.904 ± 0.028
26-08-2011	55800.383	1.3 m	15.181 ± 0.014	14.228 ± 0.014	13.564 ± 0.015	12.881 ± 0.025
09-09-2011	55814.241	1.3 m	15.174 ± 0.022	14.238 ± 0.023	13.592 ± 0.015	12.903 ± 0.032
06-11-2012	56238.259	1.3 m	14.945 ± 0.273	14.141 ± 0.237	13.496 ± 0.235	12.755 ± 0.241
29-07-2013	56503.310	1.3 m	15.185 ± 0.019	14.243 ± 0.017	13.574 ± 0.019	12.921 ± 0.022
29-08-2013	56534.329	1.3 m	15.158 ± 0.023	14.220 ± 0.022	13.528 ± 0.023	12.817 ± 0.039
20-08-2014	56890.268	1.3 m	15.176 ± 0.021	14.277 ± 0.021	13.622 ± 0.020	12.957 ± 0.027
14-09-2014	56915.333	1.3 m	15.215 ± 0.022	14.280 ± 0.014	13.609 ± 0.017	12.939 ± 0.027
22-07-2015	57226.376	1.3 m	15.224 ± 0.020	14.266 ± 0.011	13.611 ± 0.010	12.930 ± 0.012
18-11-2015	57345.193	1.3 m	15.197 ± 0.015	14.233 ± 0.013	13.554 ± 0.015	12.881 ± 0.015
06-06-2016	57546.362	1.3 m	15.167 ± 0.017	14.264 ± 0.016	13.565 ± 0.017	12.898 ± 0.029
08-09-2016	57640.269	1.3 m	15.273 ± 0.090	14.331 ± 0.084	13.679 ± 0.086	13.017 ± 0.093
06-10-2016	57668.212	1.3 m	15.230 ± 0.011	14.305 ± 0.013	13.632 ± 0.012	12.944 ± 0.013
03-11-2016	57696.223	1.3 m	15.200 ± 0.018	14.269 ± 0.019	13.604 ± 0.020	12.925 ± 0.024
25-06-2017	57930.357	1.3 m	15.208 ± 0.033	14.304 ± 0.029	13.605 ± 0.062	12.934 ± 0.072
28-08-2017	57994.355	1.3 m	15.199 ± 0.020	14.324 ± 0.017	13.713 ± 0.018	13.062 ± 0.025
13-06-2018	58283.358	1.3 m	15.188 ± 0.051	14.313 ± 0.049	13.682 ± 0.056	13.038 ± 0.070
31-07-2018	58331.345	1.3 m	15.231 ± 0.021	14.378 ± 0.017	13.752 ± 0.020	13.135 ± 0.033
13-07-2019	58678.328	1.3 m	15.224 ± 0.027	14.370 ± 0.024	13.761 ± 0.022	13.142 ± 0.036
30-07-2019	58695.300	1.3 m	15.250 ± 0.014	14.370 ± 0.014	13.741 ± 0.011	13.116 ± 0.019
11-09-2019	58738.337	1.3 m	15.272 ± 0.017	14.378 ± 0.012	13.751 ± 0.014	13.078 ± 0.022
24-06-2020	59025.375	1.3 m	15.268 ± 0.016	14.384 ± 0.009	13.763 ± 0.010	13.151 ± 0.013
19-07-2020	59050.320	1.3 m	15.312 ± 0.013	14.392 ± 0.010	13.764 ± 0.012	13.126 ± 0.021
19-08-2020	59081.323	1.3 m	15.396 ± 0.012	14.456 ± 0.010	13.806 ± 0.008	13.138 ± 0.013
04-07-2021	59400.359	1.3 m	15.266 ± 0.017	14.415 ± 0.017	13.821 ± 0.018	13.224 ± 0.022
04-09-2021	59462.354	1.3 m	15.388 ± 0.024	14.471 ± 0.021	13.816 ± 0.022	13.167 ± 0.031
10-10-2021	59498.290	1.3 m	15.465 ± 0.036	14.624 ± 0.021	14.010 ± 0.022	13.362 ± 0.026
29-07-2022	59790.379	1.3 m	15.311 ± 0.013	14.435 ± 0.010	13.840 ± 0.015	13.247 ± 0.025
17-08-2022	59809.330	1.3 m	15.296 ± 0.014	14.430 ± 0.013	13.821 ± 0.019	13.225 ± 0.020
20-09-2022	59843.312	1.3 m	15.262 ± 0.015	14.375 ± 0.013	13.776 ± 0.013	13.144 ± 0.019
29-06-2023	60125.366	1.3 m	15.357 ± 0.035	14.500 ± 0.030	13.890 ± 0.028	13.257 ± 0.025
12-07-2023	60138.348	1.3 m	15.370 ± 0.014	14.501 ± 0.015	13.892 ± 0.013	13.265 ± 0.017
23-08-2023	60180.328	1.3 m	15.291 ± 0.021	14.428 ± 0.014	13.846 ± 0.014	13.249 ± 0.020

Table B.2. Photometric observations of KS 1947+300 from 60 cm, 80 cm, 2.4 m, and YAHPT telescopes.

Date (DD-MM-YYYY)	MJD	Telescope	<i>B</i> (mag)	<i>V</i> (mag)	<i>R</i> (mag)	<i>I</i> (mag)
04-10-2013	56569.51	80cm	15.176 ± 0.028	14.261 ± 0.030	13.627 ± 0.033	12.876 ± 0.033
15-10-2013	56580.45	80cm	15.095 ± 0.024	14.175 ± 0.023	13.554 ± 0.023	12.811 ± 0.026
25-10-2013	56590.45	80cm	15.105 ± 0.009	14.198 ± 0.007	13.548 ± 0.006	12.865 ± 0.009
26-10-2013	56591.45	80cm	15.116 ± 0.009	14.203 ± 0.007	13.545 ± 0.007	12.843 ± 0.009
27-10-2013	56592.49	80cm	13.548 ± 0.020	12.842 ± 0.012
29-10-2013	56594.45	80cm	15.116 ± 0.009	14.190 ± 0.007	13.551 ± 0.007	12.841 ± 0.009
30-10-2013	56595.45	80cm	15.137 ± 0.011	14.225 ± 0.008	13.578 ± 0.007	12.860 ± 0.009
18-11-2013	56614.10	2.4m	15.096 ± 0.007	14.184 ± 0.006	13.483 ± 0.006	...
19-11-2013	56615.02	2.4m	15.094 ± 0.007	14.190 ± 0.006	13.494 ± 0.006	...
20-11-2013	56616.18	2.4m	15.100 ± 0.007	14.190 ± 0.007	13.492 ± 0.006	12.786 ± 0.009
21-11-2013	56617.77	2.4m	15.100 ± 0.007	14.190 ± 0.006	13.504 ± 0.006	12.808 ± 0.009
22-11-2013	56618.57	2.4m	15.101 ± 0.007	14.190 ± 0.006	13.500 ± 0.006	12.802 ± 0.009
23-11-2013	56619.10	2.4m	15.091 ± 0.007	14.194 ± 0.006	13.501 ± 0.006	12.791 ± 0.009
07-05-2014	56784.81	80cm	15.167 ± 0.020	14.258 ± 0.015	13.615 ± 0.012	12.930 ± 0.013
13-05-2014	56790.09	80cm	15.162 ± 0.007	14.265 ± 0.006	13.614 ± 0.006	12.906 ± 0.009
14-05-2014	56791.75	80cm	15.172 ± 0.028	14.269 ± 0.016	13.658 ± 0.016	12.940 ± 0.013
05-06-2014	56813.16	2.4m	15.189 ± 0.007	14.296 ± 0.007	13.617 ± 0.006	12.940 ± 0.009
24-06-2014	56832.95	2.4m	15.168 ± 0.011	14.301 ± 0.007
25-06-2014	56833.01	2.4m	13.632 ± 0.008	12.946 ± 0.009
27-06-2014	56835.32	2.4m	15.191 ± 0.007	14.306 ± 0.007	13.622 ± 0.006	12.940 ± 0.009
27-09-2014	56927.49	80cm	15.176 ± 0.014	14.267 ± 0.009	13.660 ± 0.009	12.990 ± 0.011
29-09-2014	56929.47	80cm	15.225 ± 0.018	14.271 ± 0.011	13.623 ± 0.011	12.937 ± 0.013
30-09-2014	56930.48	80cm	15.224 ± 0.028	14.275 ± 0.014	13.636 ± 0.012	12.961 ± 0.013
20-03-2015	57101.88	60cm	14.974 ± 0.010	14.111 ± 0.012	13.637 ± 0.018	...
22-03-2015	57103.80	60cm	15.006 ± 0.009	14.162 ± 0.009	13.667 ± 0.008	13.186 ± 0.011
23-03-2015	57104.85	60cm	14.942 ± 0.009	14.102 ± 0.009	13.595 ± 0.008	13.130 ± 0.011
07-06-2015	57180.66	80cm	15.192 ± 0.009	14.262 ± 0.008	13.617 ± 0.008	12.910 ± 0.011
01-10-2015	57296.50	80cm	15.218 ± 0.008	14.283 ± 0.007	13.630 ± 0.008	12.922 ± 0.011
02-10-2015	57297.57	80cm	15.023 ± 0.018	14.129 ± 0.010	13.668 ± 0.010	12.952 ± 0.012
03-10-2015	57298.46	80cm	15.171 ± 0.011	14.252 ± 0.008	13.586 ± 0.011	12.895 ± 0.013
04-10-2015	57299.46	80cm	15.191 ± 0.012	14.264 ± 0.009	13.599 ± 0.012	12.857 ± 0.014
05-10-2015	57300.49	80cm	15.169 ± 0.011	14.241 ± 0.009	13.572 ± 0.009	12.859 ± 0.012
08-10-2015	57303.47	80cm	...	14.292 ± 0.008	13.609 ± 0.008	12.911 ± 0.010
31-10-2015	57326.32	80cm	15.163 ± 0.009	14.247 ± 0.009	13.578 ± 0.008	12.872 ± 0.012
01-11-2015	57327.12	80cm	15.176 ± 0.012	14.247 ± 0.011	13.567 ± 0.010	12.877 ± 0.013
13-11-2015	57339.09	2.4m	13.583 ± 0.006	12.885 ± 0.009
29-11-2015	57355.51	80cm	15.170 ± 0.014	14.211 ± 0.009	13.577 ± 0.010	12.872 ± 0.011
30-11-2015	57356.50	80cm	15.180 ± 0.045	14.225 ± 0.020	13.541 ± 0.018	12.873 ± 0.018
19-09-2016	57650.52	60cm	15.154 ± 0.009	14.260 ± 0.008	13.601 ± 0.007	12.898 ± 0.011
20-09-2016	57651.52	60cm	15.085 ± 0.008	14.251 ± 0.009	13.597 ± 0.008	12.903 ± 0.011
27-09-2016	57658.52	60cm	15.178 ± 0.009	14.285 ± 0.009	13.576 ± 0.010	12.888 ± 0.013
28-09-2016	57659.54	60cm	15.137 ± 0.011	14.253 ± 0.008	13.581 ± 0.008	12.898 ± 0.012
25-10-2016	57686.51	60cm	15.177 ± 0.012	14.272 ± 0.010	13.566 ± 0.010	12.903 ± 0.013
29-10-2016	57690.53	60cm	13.598 ± 0.009	12.900 ± 0.012
30-10-2016	57692.55	60cm	15.190 ± 0.010	14.282 ± 0.010	13.581 ± 0.009	12.908 ± 0.012
23-11-2016	57715.49	60cm	13.635 ± 0.009	12.930 ± 0.013
01-12-2016	57723.48	60cm	15.157 ± 0.009	14.295 ± 0.009	13.589 ± 0.010	12.916 ± 0.013
15-09-2017	58011.54	80cm	15.224 ± 0.009	14.341 ± 0.008	13.706 ± 0.008	13.030 ± 0.011
17-09-2017	58013.57	80cm	15.214 ± 0.008	14.341 ± 0.008	13.696 ± 0.007	13.027 ± 0.011
18-09-2017	58014.53	80cm	15.233 ± 0.008	14.340 ± 0.008	13.702 ± 0.008	13.042 ± 0.010
19-09-2017	58015.54	80cm	15.217 ± 0.010	14.355 ± 0.009	13.725 ± 0.010	13.097 ± 0.013
20-09-2017	58016.52	80cm	15.235 ± 0.010	14.361 ± 0.009	13.725 ± 0.008	13.071 ± 0.012
27-10-2017	58053.48	60cm	15.217 ± 0.012	14.323 ± 0.011	13.678 ± 0.011	13.006 ± 0.014
28-10-2017	58054.48	60cm	15.240 ± 0.015	14.385 ± 0.012	13.759 ± 0.011	13.048 ± 0.015
29-10-2017	58055.48	60cm	15.198 ± 0.012	14.324 ± 0.011	13.684 ± 0.010	13.023 ± 0.013
30-10-2017	58056.47	60cm	15.197 ± 0.012	14.334 ± 0.009	13.683 ± 0.010	13.025 ± 0.012
19-11-2017	58076.44	60cm	15.161 ± 0.011	14.307 ± 0.010	13.671 ± 0.009	13.012 ± 0.015

Table B.3. Photometric observations of KS 1947+300 from 60 cm , 80 cm, 2.4 m, and YAHPT telescopes—continued.

Date (DD-MM-YYYY)	MJD	Telescope	<i>B</i> (mag)	<i>V</i> (mag)	<i>R</i> (mag)	<i>I</i> (mag)
20-11-2017	58077.42	60cm	15.200 ± 0.009	14.324 ± 0.008	13.674 ± 0.009	13.020 ± 0.013
21-11-2017	58078.46	60cm	15.196 ± 0.011	14.326 ± 0.010	13.682 ± 0.010	13.026 ± 0.014
22-11-2017	58079.45	60cm	15.203 ± 0.011	14.306 ± 0.012	13.677 ± 0.009	13.071 ± 0.050
23-11-2017	58080.48	60cm	15.181 ± 0.011	14.317 ± 0.009	13.673 ± 0.008	13.033 ± 0.011
08-09-2018	58369.59	80cm	15.249 ± 0.010	14.348 ± 0.008	13.722 ± 0.007	13.077 ± 0.010
09-09-2018	58370.53	80cm	15.251 ± 0.010	14.359 ± 0.008	13.736 ± 0.007	13.109 ± 0.010
16-09-2018	58377.52	80cm	15.240 ± 0.008	14.337 ± 0.007	13.712 ± 0.007	13.057 ± 0.010
08-11-2018	58430.47	80cm	15.266 ± 0.009	14.378 ± 0.008	13.767 ± 0.008	13.135 ± 0.011
24-09-2019	58750.52	80cm	15.318 ± 0.008	14.439 ± 0.007	13.806 ± 0.007	13.173 ± 0.009
25-09-2019	58751.52	80cm	15.297 ± 0.008	14.405 ± 0.007	13.780 ± 0.007	13.141 ± 0.009
04-10-2019	58760.49	80cm	15.366 ± 0.009	14.476 ± 0.009	13.858 ± 0.008	13.212 ± 0.011
03-11-2019	58790.47	80cm	15.274 ± 0.010	14.390 ± 0.008	13.788 ± 0.007	13.161 ± 0.010
04-11-2019	58791.45	80cm	15.274 ± 0.009	14.401 ± 0.008	13.792 ± 0.007	13.160 ± 0.010
15-09-2020	59107.59	80cm	15.443 ± 0.009	14.540 ± 0.008	13.885 ± 0.007	13.211 ± 0.011
16-09-2020	59108.53	80cm	15.450 ± 0.009	14.557 ± 0.008	13.912 ± 0.007	13.255 ± 0.010
09-10-2020	59131.49	80cm	15.422 ± 0.014	14.642 ± 0.011	13.921 ± 0.009	13.289 ± 0.011
12-10-2020	59134.49	80cm	15.422 ± 0.009	14.553 ± 0.008	13.938 ± 0.007	13.318 ± 0.009
20-11-2020	59173.50	80cm	15.341 ± 0.022	14.473 ± 0.026	13.889 ± 0.028	13.207 ± 0.032
22-11-2020	59175.42	80cm	15.313 ± 0.012	14.449 ± 0.009	13.854 ± 0.008	13.242 ± 0.011
21-12-2020	59204.44	80cm	15.263 ± 0.012	14.392 ± 0.010	13.812 ± 0.008	13.193 ± 0.011
10-10-2021	59497.50	80cm	15.485 ± 0.011	14.612 ± 0.008	13.987 ± 0.008	13.361 ± 0.011
12-10-2022	59864.62	YAHPT	15.275 ± 0.009	14.375 ± 0.007	13.773 ± 0.018	13.157 ± 0.024
13-10-2022	59865.51	YAHPT	15.262 ± 0.006	14.373 ± 0.006	13.754 ± 0.006	13.144 ± 0.009
18-10-2022	59870.65	YAHPT	15.372 ± 0.097	14.107 ± 0.107	13.618 ± 0.120	...
20-10-2022	59872.50	YAHPT	15.264 ± 0.006	14.373 ± 0.006	13.757 ± 0.006	13.151 ± 0.009
22-10-2022	59874.50	YAHPT	15.271 ± 0.006	14.376 ± 0.006	13.758 ± 0.006	13.153 ± 0.009
28-10-2022	59880.65	YAHPT	15.279 ± 0.007	14.377 ± 0.006	13.738 ± 0.006	13.121 ± 0.010
29-10-2022	59881.64	YAHPT	15.268 ± 0.007	14.362 ± 0.006	13.741 ± 0.006	13.133 ± 0.009
30-10-2022	59882.60	YAHPT	15.285 ± 0.007	14.366 ± 0.006	13.744 ± 0.006	13.140 ± 0.009
01-11-2022	59884.59	YAHPT	15.292 ± 0.007	14.386 ± 0.006	13.752 ± 0.006	13.149 ± 0.009
02-11-2022	59885.63	YAHPT	15.275 ± 0.008	14.380 ± 0.007	13.741 ± 0.007	13.121 ± 0.010
03-11-2022	59886.62	YAHPT	15.267 ± 0.008	14.379 ± 0.007	13.757 ± 0.007	13.134 ± 0.010
06-11-2022	59889.63	YAHPT	15.268 ± 0.011	14.358 ± 0.008	13.747 ± 0.007	13.101 ± 0.011
07-11-2022	59890.62	YAHPT	15.287 ± 0.016	14.352 ± 0.009	13.715 ± 0.009	13.087 ± 0.013
08-11-2022	59891.62	YAHPT	15.271 ± 0.017	14.394 ± 0.009	13.745 ± 0.009	13.125 ± 0.013
09-11-2022	59892.61	YAHPT	15.273 ± 0.016	14.358 ± 0.008	13.727 ± 0.007	13.120 ± 0.011
10-11-2022	59893.62	YAHPT	15.277 ± 0.012	14.368 ± 0.008	13.733 ± 0.008	13.069 ± 0.012
12-11-2022	59895.61	YAHPT	15.285 ± 0.010	14.374 ± 0.008	13.748 ± 0.007	13.095 ± 0.011
15-11-2022	59898.60	YAHPT	15.291 ± 0.008	14.385 ± 0.007	13.758 ± 0.007	13.116 ± 0.010
17-11-2022	59900.60	YAHPT	15.292 ± 0.008	14.384 ± 0.007	13.742 ± 0.007	13.121 ± 0.010
20-11-2022	59903.50	YAHPT	15.303 ± 0.006	14.411 ± 0.006	13.783 ± 0.006	13.164 ± 0.009
21-11-2022	59904.49	YAHPT	15.306 ± 0.006	14.416 ± 0.006	13.786 ± 0.006	13.167 ± 0.009
24-11-2022	59907.50	YAHPT	15.316 ± 0.007	14.420 ± 0.006	13.792 ± 0.006	13.168 ± 0.009
25-11-2022	59908.49	YAHPT	15.310 ± 0.006	14.422 ± 0.006	13.793 ± 0.006	13.165 ± 0.009
27-11-2022	59910.50	YAHPT	15.308 ± 0.007	14.420 ± 0.006	13.784 ± 0.006	13.177 ± 0.009
28-11-2022	59911.49	YAHPT	15.316 ± 0.007	14.424 ± 0.006	13.793 ± 0.006	13.161 ± 0.009
01-12-2022	59914.49	YAHPT	15.321 ± 0.007	14.438 ± 0.006	13.807 ± 0.006	13.199 ± 0.009
02-12-2022	59915.49	YAHPT	15.328 ± 0.007	14.440 ± 0.006	13.815 ± 0.006	13.207 ± 0.010
03-12-2022	59916.56	YAHPT	15.301 ± 0.012	14.402 ± 0.008	13.782 ± 0.007	13.178 ± 0.011
05-12-2022	59918.49	YAHPT	15.313 ± 0.008	14.440 ± 0.007	13.819 ± 0.007	13.191 ± 0.010
06-12-2022	59919.48	YAHPT	15.304 ± 0.008	14.427 ± 0.007	13.616 ± 0.083	13.209 ± 0.010
07-12-2022	59920.52	YAHPT	15.314 ± 0.011	14.420 ± 0.007	13.815 ± 0.007	13.210 ± 0.011
08-12-2022	59921.52	YAHPT	15.297 ± 0.012	14.421 ± 0.009	13.825 ± 0.008	13.230 ± 0.014
09-12-2022	59922.49	YAHPT	15.319 ± 0.008	14.434 ± 0.007	13.812 ± 0.007	13.201 ± 0.010